



Superconductivity with high upper critical field in Ta-Hf alloys

P. K. Meena, S. Jangid, R. K. Kushwaha , and R. P. Singh *

Department of Physics, Indian Institute of Science Education and Research Bhopal, Bhopal 462066, India

 (Received 27 May 2023; accepted 1 August 2023; published 18 August 2023)

High upper-critical field superconducting alloys are required for superconducting device applications. In this paper, we extensively characterized the structure and superconducting properties of alloys $\text{Ta}_x\text{Hf}_{1-x}$ ($x = 0.2, 0.4, 0.5, 0.6$ and 0.8). The substitution of Hf ($T_C = 0.12$ K, type-I superconductor) with Ta ($T_C = 4.4$ K, type-I superconductor) shows an anomalous enhancement of T_C with a variation of composition. Interestingly, all compositions exhibited strongly coupled bulk type-II superconductivity with a high upper critical field.

DOI: [10.1103/PhysRevMaterials.7.084801](https://doi.org/10.1103/PhysRevMaterials.7.084801)

I. INTRODUCTION

Superconductivity, a quantum phenomenon with significant practical applications, has recently led to the exploration of unconventional superconductors that exhibit remarkable properties that differ from the conventional BCS model [1]. These unconventional superconductors exhibit remarkable features, such as an upper critical field comparable to or exceeding the Pauli paramagnetic field, strong electron-phonon interactions, the presence of gap nodes, and the breaking of the time-reversal symmetry [2,3]. The strength of spin-orbit coupling (SOC) plays a pivotal role in the emergence of unconventional superconductivity [4–10]. Superconductors based on heavier elements with higher atomic numbers, particularly those in the $5d$ series, tend to exhibit robust SOC $\propto Z^4$, giving rise to these unconventional superconducting behaviors [11–24].

The Ta-Hf binary alloy is a notable example of a $5d$ superconducting alloy that combines two type-I elemental superconductors, namely, Ta and Hf. Due to the high atomic numbers of its constituent elements, it is expected to display strong spin-orbit coupling, which can be tuned through substitutions. Introducing Hf, with a T_C (superconducting transition temperature) of 0.12 K, into Ta, with a T_C of 4.4 K, results in a remarkable increase in the superconducting transition temperature of the Hf-Ta alloy, reaching 6.7 K with approximately 40% Hf [25,26]. Additionally, this alloy demonstrates a surprising enhancement in the upper critical field [27]. The relationship between the density of states at the Fermi level, the electron-phonon coupling, and the number of valence electrons (d shell) per atom has been correlated with the superconducting transition temperature (T_C) [28,29]. However, T_C exhibits nonmonotonic behavior with valence electron counts, a trend observed in other binary alloy superconductors [28,30–36]. These metallic alloys possess both metallic properties and a high upper critical field, making them highly promising for practical superconducting devices [37].

Despite studies on Ta-Hf binary alloys [38,39], the mechanisms responsible for the enhanced critical temperature (T_C)

and the high upper critical field behavior in these alloys have not been fully understood, primarily due to incomplete characterization. Unraveling these mechanisms could provide valuable insight and enable the synthesis of metallic alloys with enhanced properties suitable for practical applications. Thus, the Ta-Hf alloy is a promising candidate for in-depth investigations into its superconducting properties, offering a platform to better comprehend other binary superconducting behaviors.

In this paper, we investigate the superconducting properties of the binary alloys $\text{Ta}_x\text{Hf}_{1-x}$ ($x = 0.2, 0.4, 0.5, 0.6,$ and 0.8). Our analysis included electrical resistivity, DC magnetization, and heat-capacity measurements, allowing us to construct the phase diagram for these alloys. Throughout the entire range of the solid solution, we observed the coexistence of two crystal structures: *W-bcc* and *Mg-hcp*. Notably, all compositions of $\text{Ta}_x\text{Hf}_{1-x}$ exhibited bulk type-II strongly coupled superconductivity having an upper critical field comparable to the Pauli limiting field.

II. EXPERIMENTAL DETAILS

Polycrystalline samples of $\text{Ta}_x\text{Hf}_{1-x}$ were prepared by arc melting using Ta (4N) and Hf (4N) metals in stoichiometric ratios in a high purity Ar (4N) environment on a water-cooled copper hearth. The ingots were repeatedly remelted and flipped to enhance chemical homogeneity with minimal mass loss. A titanium button was used as a getter to remove residual oxygen from the chamber. The crystal structure and phase purity were verified using powder x-ray diffraction (XRD) on a analytical diffractometer equipped with $\text{Cu } K\alpha$ radiation ($\lambda = 1.54056$ Å). Magnetization measurements were performed using the magnetic property measurement system 3 (Quantum Design). Specific heat and electrical resistivity measurements were performed using the physical property measurement system (Quantum Design).

III. EXPERIMENTAL RESULTS

A. Sample characterization

All synthesized binary alloys $\text{Ta}_x\text{Hf}_{1-x}$ ($x = 0.2, 0.4, 0.5, 0.6,$ and 0.8) are found to be in a pure phase and crystallize

*rpsingh@iiserb.ac.in

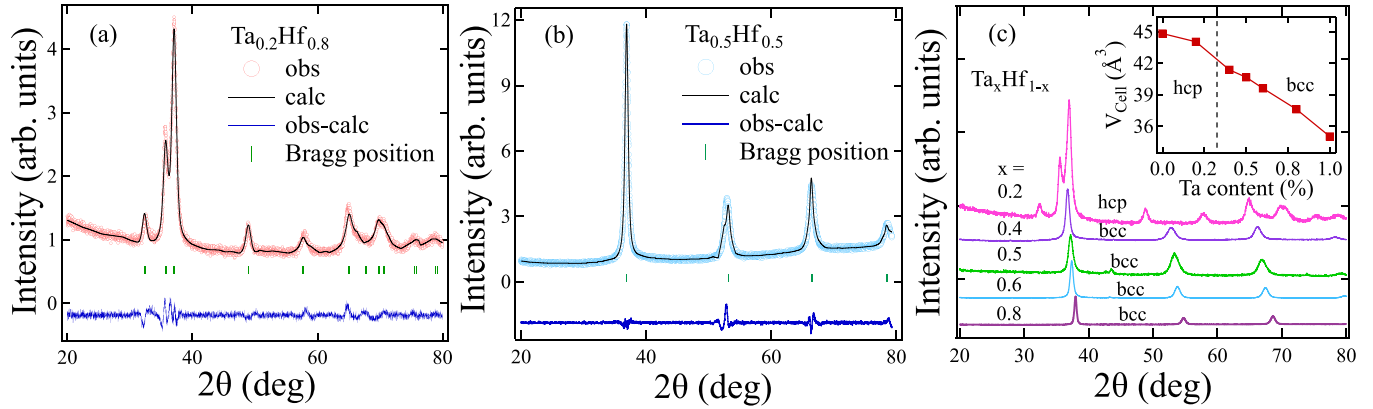


FIG. 1. Powder XRD patterns with refinement for binary alloys, (a) $\text{Ta}_{0.2}\text{Hf}_{0.8}$. (b) $\text{Ta}_{0.5}\text{Hf}_{0.5}$. (c) All compositions XRD patterns for $\text{Ta}_x\text{Hf}_{1-x}$. The inset shows the refined cell volume as a function of the Ta content x .

into two distinct crystal structures. Figures 1(a) and 1(b) show representative XRD patterns for polycrystalline binary alloys with $x = 0.2$ and 0.5 , whereas, the XRD patterns of other alloys closely resemble those of $x = 0.5$. We used FULL-PROF RIETVELD software [40] to analyze the XRD patterns, revealing that the samples can be well indexed by the *Mg-hcp* structure with space-group $P6_3/mmc$ for $x = 0.2$ and the *W-bcc* structure with space-group $Im\bar{3}m$ for the remaining compositions. Figure 1(c) displays the XRD patterns for all compounds ($x = 0.2, 0.4, 0.5, 0.6$, and 0.8), whereas, the refined structural lattice parameters for these compounds are

summarized in Table I. The lattice constants obtained for some binary compounds are consistent with previous studies in the literature [41], whereas others are reported for the first time in this paper. The inset of Fig. 1(c) shows a linear decrease in V_{cell} with increasing x , which can be attributed to the smaller atomic radius of Ta compared to Hf.

B. Superconducting and normal-state properties

Superconductivity in the binary alloys $\text{Ta}_x\text{Hf}_{1-x}$ ($x = 0.2, 0.4, 0.5, 0.6$, and 0.8) was confirmed by measurements

TABLE I. $\text{Ta}_x\text{Hf}_{1-x}$ ($x = 0.2-0.8$) Space group, refined lattice parameters, and cell volume derived from x-ray refinement as well as superconducting and normal-state parameters derived from magnetization, resistivity, and specific-heat measurements.

Parameter	Unit	0.2	0.4	0.5	0.6	0.8
Space group		$P6_3/mmc$		$Im\bar{3}m$		
$a = b$	Å	3.1849	3.4586	3.4392	3.4034	3.3509
c	Å	5.0143	3.4586	3.4392	3.4034	3.3509
V_{cell}	Å ³	44.05	41.37	40.67	39.62	37.62
T_C	K	4.5	5.6	6.1	6.7	6.6
$H_{C1}(0)$	mT	23.52	26.40	23.87	22.6	22.51
$H_{C2}^{\text{res}}(0)$	T	7.72	10.43	9.3	9.27	5.69
$H_{C2}^{\text{p}}(0)$	T	8.28	10.30	11.22	12.32	12.14
$H_{C2}^{\text{orb}}(0)$	T	3.34	5.89	6.77	6.30	3.68
α_m		0.56	0.80	0.82	0.72	0.43
ξ_{GL}	nm	6.52	5.62	5.95	5.96	7.60
$\lambda_{GL}^{\text{mag}}$	nm	150.74	144.64	151.93	156.84	149.19
k_{GL}		23.07	25.73	25.53	26.31	19.63
$\rho_{300\text{K}}/\rho_{8\text{K}}(\text{RRR})$		1.48	1.02	1.11	1.20	1.59
γ_n	$\text{mJ mol}^{-1} \text{K}^{-2}$	4.7	6.6	8.9	9.3	8.0
θ_D	K	166.6	158.7	151.6	222.3	256.2
$\frac{\Delta_{sp}(0)}{k_B T_C}$		1.87	2.56	2.45	2.38	2.07
λ_{e-ph}		0.76	0.85	0.89	0.81	0.74
$\frac{m^*}{m_e}$		0.74	0.91	1.10	1.13	1.02
v_f	10^5 ms^{-1}	7.13	6.69	6.14	6.06	6.64
$\frac{\xi_0}{l_e}$		2.5	3.0	4.0	2.4	4.1
T_F	10^4 K	1.23	1.33	1.35	1.36	1.44

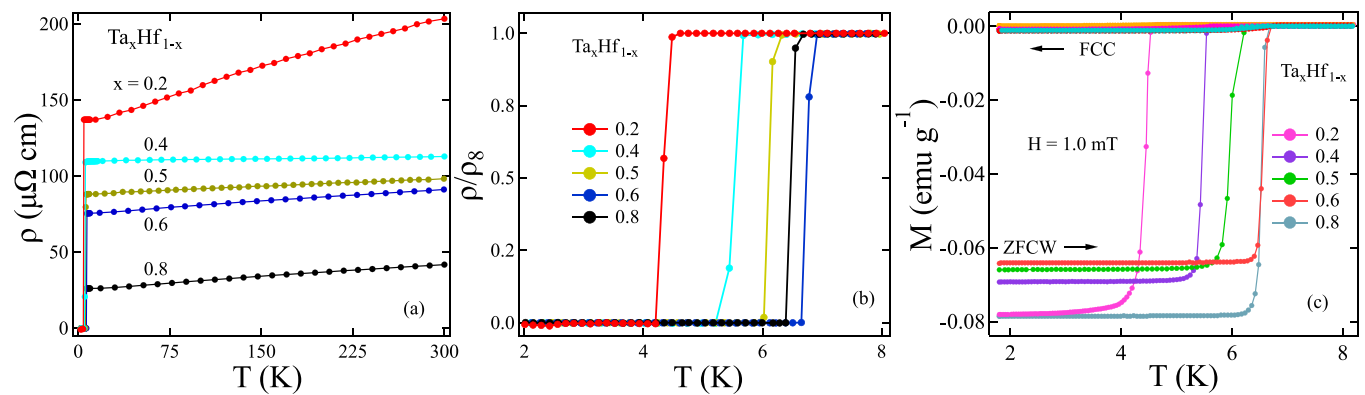


FIG. 2. (a) Temperature variation of electrical resistivity $\rho(T)$ at $H = 0$ mT for $\text{Ta}_x\text{Hf}_{1-x}$ ($x = 0.2, 0.4, 0.5, 0.6,$ and 0.8). (b) A zoomed-in view of the normalized resistivity (ρ/ρ_8) highlights the superconducting drop observed in all compositions. (c) Magnetization data obtained during field-cooled cooling (FCC) and zero field-cooled heating (ZFCW) measurements in an applied field of $H = 1.0$ mT show the presence of superconductivity below T_C for all binary $\text{Ta}_x\text{Hf}_{1-x}$ compositions.

of electrical resistivity and DC magnetization. Temperature-dependent electrical resistivity [$\rho(T)$] was measured from 300 to 1.9 K at zero magnetic field ($H = 0$ mT) as shown in Fig. 2(a). The resistivity exhibited a slight temperature variation above the superconducting transition temperature (T_C), indicating the weak metallic character of the Ta-Hf alloys [42,43]. The values of the residual resistivity ratio (RRR), defined as the ratio of resistivity at 300 K to that at 8 K, were found to be relatively small (RRR $\simeq 1$ and 2) for all compositions, suggesting the presence of disorder in the binary alloy. The RRR values follow a similar pattern observed in other binary alloys [44] and are provided in Table I.

Figure 2(b) presents an expanded plot of the normalized electrical resistivity data at zero field, clearly showing the superconducting transitions corresponding to different compositions of the Ta-Hf alloy. The superconducting transition temperature (T_C) varies nonlinearly with the Hf (or Ta) concentration, ranging from 0.12 K for pure Hf to 6.7 K for a Ta concentration of 60% in a solid solution with a T_C of 4.4 K for pure Ta.

The magnetic moment variations with temperature were measured at an applied field of 1.0 mT using two different modes: ZFCW and FCC. Magnetization data for all samples exhibited the emergence of diamagnetic behavior at different transition temperatures (T_C), consistent with resistivity measurements, as shown in Fig. 2(c). The Ta-Hf binary alloy displayed a distinct dome-shaped behavior, similar to that observed in the Ti-V [45] and Zr-Nb [46] binary alloys. The maximum and minimum T_C values of 6.7 and 4.5 K were observed for compositions corresponding to 60% and 20% Ta concentration, respectively. The separation between the ZFCW and the FCC modes in the magnetization data below T_C indicates a strong magnetic flux pinning. The respective T_C values obtained from the DC magnetization consistent with the electrical transport measurements and values are summarized in Table I.

Magnetization versus field (M - H) measurements were conducted for $\text{Ta}_x\text{Hf}_{1-x}$ alloys to confirm their type-II behavior. Figure 3(a) displays the M - H curves for $x = 0.4, 0.5,$ and 0.6 , revealing the presence of the fishtail effect. The compo-

sition $x = 0.5$ also exhibits a flux jump in the magnetization loop. These unconventional vortex states, typically observed in high- T_C oxides and certain two-dimensional superconducting materials [47–50], suggest the influence of strong disorder in the material.

The lower critical field $H_{C1}(0)$ was estimated by measuring the low-field M - H . The temperature dependence of H_{C1} is determined by identifying the point at which the $M(H)$ curves deviate from the Meissner line as shown in the inset of Fig. 3(b) for $\text{Ta}_{0.5}\text{Hf}_{0.5}$. The temperature variation of the H_{C1} values for all compositions is presented in Fig. 3(b). Utilizing the Ginzburg-Landau (GL) theory of phase transition, $H_{C1}(0)$ values for $\text{Ta}_x\text{Hf}_{1-x}$ can be obtained by fitting the expression for $H_{C1}(T)$,

$$H_{C1}(T) = H_{C1}(0) \left[1 - \left(\frac{T}{T_C} \right)^2 \right]. \quad (1)$$

The estimated $H_{C1}(0)$ is in the range of 20–30 mT for all compositions of $\text{Ta}_x\text{Hf}_{1-x}$ ($x = 0.2, 0.4, 0.5, 0.6,$ and 0.8).

Temperature-dependent magnetization and resistivity data were also taken in external magnetic fields up to 7.0 and 9.0 T, respectively, to determine the upper critical field $H_{C2}(0)$. The observed changes in T_C with an increasing applied magnetic field as shown in the inset of Fig. 3(c) for $\text{Ta}_{0.5}\text{Hf}_{0.5}$, are interpreted as the upper critical field $H_{C2}(T)$. Temperature-dependent H_{C2} data were fitted using GL expression for the respective compositions to determine the $H_{C2}(0)$ values as given in Eq. (2), and the fitting is shown by solid lines in Fig. 3(c),

$$H_{C2}(T) = H_{C2}(0) \left[\frac{(1-t^2)}{(1+t^2)} \right], \quad \text{where } t = \frac{T}{T_C}. \quad (2)$$

The estimated $H_{C2}(0)$ values through aforementioned measurements are given in Table I for all the composite alloys. Maximum $H_{C2}(0)$ values are obtained as 10.43 T for $\text{Ta}_{0.4}\text{Hf}_{0.6}$ and exhibit a steady decrease with increasing Ta content in replacement of Hf content [38,51].

In type-II superconductors, the presence of a magnetic field leads to the destruction of superconductivity due to two

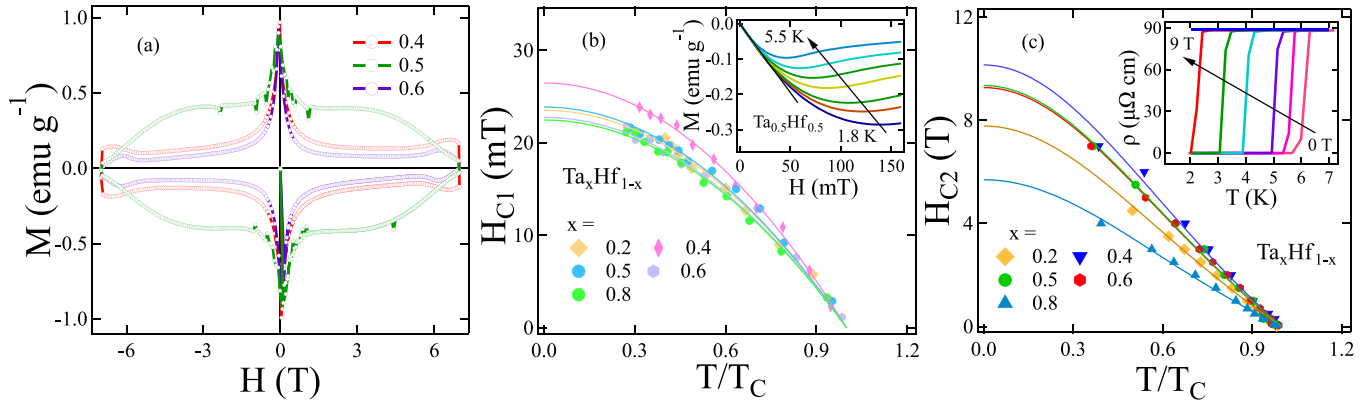


FIG. 3. (a) The magnetization of $\text{Ta}_x\text{Hf}_{1-x}$ alloys was measured in the magnetic-field range of -7 to 7 T. The fishtail effect near a magnetic field of 6 T is evident in the data. (b) The temperature dependence of the lower critical field (H_{C1}) was determined from magnetization measurements. The H_{C1} values were fitted using the GL equation for $\text{Ta}_x\text{Hf}_{1-x}$ alloys. The inset shows the magnetization curve [$M(H)$] for $\text{Ta}_{0.5}\text{Hf}_{0.5}$ at various temperatures. (c) The temperature dependence of the upper critical field (H_{C2}) was obtained from resistivity measurements. The H_{C2} values were fitted using the GL equation. The inset shows the temperature-dependent resistivity [$\rho(T)$] for $\text{Ta}_{0.5}\text{Hf}_{0.5}$ at different magnetic fields.

main effects: the orbital limiting field and the Pauli paramagnetic field. In situations where both effects are significant, the temperature dependence of the upper critical field can be described by the Werthamer-Helfand-Hohenberg (WHH) theory. This theory considers the combined influences of spin paramagnetism and spin-orbit interaction. In the absence of Pauli spin paramagnetism and the spin-orbit interaction, the WHH theory provides the following equation [52,53]:

$$H_{C2}^{\text{orb}}(0) = -\alpha T_C \left. \frac{dH_{C2}(T)}{dT} \right|_{T=T_C}, \quad (3)$$

which gives the orbital limit field of the Cooper pair. The constant α , is the purity factor of $0.693(0.73)$ for dirty(clean) limit superconductors. For the dirty limit condition, we obtained the $H_{C2}^{\text{orb}}(0)$ values, which are summarized in Table I. But the latter λ_{SO} has been shown to increase with increasing atomic numbers of the composing elements [39] and is, thus, expected to be high for $\text{Ta}_x\text{Hf}_{1-x}$, so the spin-orbit scattering effect cannot be ignored. However, the Pauli limit of the upper critical field [54,55], can be calculated by following relation $H_{C2}^p(0) = 1.84T_C$ within the BCS theory. We calculated the $H_{C2}^p(0)$ values using the estimated T_C of the resistivity curves as $8.28, 10.34, 11.59, 12.32,$ and 12.14 T for $\text{Ta}_x\text{Hf}_{1-x}$ ($x = 0.2, 0.4, 0.5, 0.6,$ and 0.8). Interestingly, the value of $H_{C2}(0)$ is comparable to Pauli's limiting field for $x = 0.2, 0.4$, indicating the unconventionality present in these compounds. Similar results have been observed in certain superconductors, including Chevrel phase [56], A15 compounds [57], and various rhenium- (Re-) based noncentrosymmetric superconductors [58–60]. However, further investigations using low-temperature-high magnetic-field measurements on single-crystalline samples are imperative to determine these parameters precisely.

To further quantify the impact of spin paramagnetic effects, we calculated the Maki parameter (α_m), which is given in the following expression:

$$\alpha_m = \sqrt{2} \frac{H_{C2}^{\text{orb}}(0)}{H_{C2}^p(0)}. \quad (4)$$

The calculated values of α_m are provided in Table I. The observed variation of α_m with doping can be attributed to the interplay between spin-orbit coupling and doping-induced disorder, arising from differences in atomic numbers (Z) and atomic radii of the constituent elements in the Ta-Hf alloy.

Two length scales of characteristics of a superconductor were determined: penetration depth $\lambda_{GL}(0)$ and Ginzburg-Landau coherence length $\xi_{GL}(0)$ from the given relations using the value of $H_{C1}(0)$ and $H_{C2}(0)$,

$$H_{C2}(0) = \frac{\Phi_0}{2\pi \xi_{GL}^2(0)}, \quad (5)$$

$$H_{C1}(0) = \frac{\Phi_0}{4\pi \lambda_{GL}^2(0)} \left(\ln \frac{\lambda_{GL}(0)}{\xi_{GL}(0)} + 0.12 \right), \quad (6)$$

where Φ_0 denotes the fluxoid quantum ($\Phi_0 = 2.07 \times 10^{-15} \text{ T m}^2$) [61]. Subsequently, the GL parameter is defined as $k_{GL} = \frac{\lambda_{GL}(0)}{\xi_{GL}(0)}$, which signifies the type of superconductivity (either I or II), was also calculated for each composition. Moreover, the relation $H_{C1}(0)H_{C2}(0) = H_C^2(0) \ln[k_{GL}(0) + 0.08]$ can be used to compute thermodynamic critical field H_C at 0 K using the value of $H_{C1}(0)$, $H_{C2}(0)$, and k_{GL} . The obtained values of H_C are 190 – 300 mT for all compositions. All physical parameters $\xi_{GL}(0)$, $\lambda_{GL}(0)$, and k_{GL} are summarized in Table I. The estimated values of $\xi_{GL}(0)$ and $\lambda_{GL}(0)$ are in the range of 5 – 8 nm and 140 – 160 nm, respectively, same as Re-doped MoTe_2 [62], Ru- and Ir-doped LaRu_3Si_2 [63]. The large values of k_{GL} in the range of 23 – 27 [64] for binary compounds, suggests that $\text{Ta}_x\text{Hf}_{1-x}$ have strong type-II superconductivity.

Heat-capacity measurements were conducted for all compositions to further characterize superconductivity in $\text{Ta}_x\text{Hf}_{1-x}$ alloys. As depicted in Fig. 4, the heat-capacity plots exhibit a discontinuity that signifies the transition from normal to superconducting state. The determined T_C values of specific heat are consistent with all the resistivity and magnetization measurements of the compounds. Low-temperature specific heat can be described using the Debye relation, $C = \gamma_n T + \beta_3 T^3 + \beta_5 T^5$, where the term $\gamma_n T$ represents the electronic

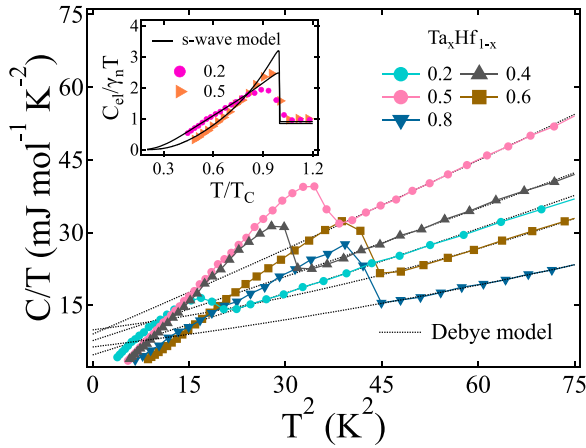


FIG. 4. C/T versus T^2 measured at $H = 0$ mT and fitted in normal state using relation $C = \gamma_n T + \beta_3 T^3 + \beta_5 T^5$. The inset shows normalized electronic specific heat, which is well described with the isotropic BCS model.

contribution, and the term $\beta_3 T^3$ corresponds to the phononic contribution, whereas $\beta_5 T^5$ corresponds to the anharmonic contribution. By extrapolating the behavior of the normal state to low temperatures, the Sommerfeld coefficient (γ_n), the Debye constant (β_3), and the anharmonic constant β_5 can be estimated.

Using the known value of β_3 , the Debye temperature θ_D can be calculated using the expression $\theta_D = (\frac{12\pi^4 R n}{5\beta_3})^{1/3}$, where R is the universal gas constant ($8.314 \text{ J K}^{-1} \text{ mol}^{-1}$) and $n = 1$ is the number of atoms per unit cell. The density of states at the Fermi level, denoted as $D(E_F)$, can be determined using the relation $D(E_F) = \frac{3\gamma_n}{\pi^2 k_B}$, where k_B is the Boltzmann constant [65]. By applying these equations, the calculated values of θ_D are lower than the Debye temperature of the corresponding elements. Furthermore, as the concentration increases up to 50% of the Ta content, the values of θ_D decrease, indicating that doping introduces some disorder in binary alloys. The values obtained from θ_D are provided in Table I. Subsequently, we determined the electron-phonon coupling constant, denoted as λ_{e-ph} . This dimensionless constant quantifies the attractive interaction between electrons and phonons and can be calculated using the values of T_C and θ_D through the semiempirical McMillan formula [66],

$$\lambda_{e-ph} = \frac{1.04 + \mu^* \ln(\theta_D/1.45T_C)}{(1 - 0.62\mu^*) \ln(\theta_D/1.45T_C) - 1.04}, \quad (7)$$

where the repulsive screened Coulomb parameter, denoted as μ^* , typically falls within the range of 0.09–0.18 with a commonly used value of 0.13 for intermetallic compounds. In our case, we adopted a value of 0.13. The estimated values of λ_{e-ph} for $\text{Ta}_x\text{Hf}_{1-x}$ alloys ranging from 0.7 to 1 as summarized in Table I. Similar values of λ_{e-ph} have been observed in other binary compounds, such as $\text{Re}_{1-x}\text{Mo}_x$ [67]. The higher values of λ_{e-ph} in $\text{Ta}_x\text{Hf}_{1-x}$ alloys indicate a strong coupling strength among electrons in the superconducting state [68].

The inset of Fig. 4 presents the electronic component of the specific heat, denoted as C_{el} (shown for $x = 0.2$ and 0.5), which was obtained by subtracting the contribution of the

phonon from the experimental data using the relation $C_{el}(T) = C - \beta_3 T^3 - \beta_5 T^5$. The $C_{el}(T)$ data for all compositions are well described by the isotropic s-wave model in the BCS theory, as outlined in Ref. [69]. The black line in the inset of Fig. 4 represents the curve fitted to the data using the single-gap s-wave BCS equation. The values obtained from the superconducting gap ($\frac{\Delta(0)}{k_B} T_C$), listed in Table I, exceed the predicted BCS value, indicating the presence of strongly coupled superconductivity in $\text{Ta}_x\text{Hf}_{1-x}$ compounds.

C. Electronic properties

The Sommerfeld coefficient γ_n , is related to the effective mass of quasiparticles m^* and electronic carrier density n of the system by the following expression [65]:

$$\gamma_n = \left(\frac{\pi}{3}\right)^{2/3} \frac{k_B^2 m^* V_{f.u.} n^{1/3}}{\hbar^2 N_A}, \quad (8)$$

where $k_B = 1.38 \times 10^{-23} \text{ J/K}$ is the Boltzmann's constant, N_A and $V_{f.u.}$ are the Avogadro number and the volume of a formula unit, respectively. The following relations can be used to connect the electronic mean free path l_e and the carrier density n to the Fermi velocity v_F and the effective mass m^* ,

$$l_e = \frac{3\pi^2 \hbar^3}{e^2 \rho_0 m^{*2} v_F^2}, \quad n = \frac{1}{3\pi^2} \left(\frac{m^* v_F}{\hbar}\right)^3. \quad (9)$$

In the dirty limit, the GL penetration depth $\lambda_{GL}(0)$ and coherence length $\xi_{GL}(0)$ get affected, which can be described in terms of London penetration depth (λ_L) and BCS coherence length (ξ_0) by the following modified Eqs. (10) and (11), respectively,

$$\lambda_{GL}(0) = \lambda_L \left(1 + \frac{\xi_0}{l_e}\right)^{1/2}, \quad \lambda_L = \left(\frac{m^*}{\mu_0 n e^2}\right)^{1/2}, \quad (10)$$

$$\frac{\xi_{GL}(0)}{\xi_0} = \frac{\pi}{2\sqrt{3}} \left(1 + \frac{\xi_0}{l_e}\right)^{-1/2} \quad (11)$$

The above set of Eqs. (8)–(11) were solved simultaneously as performed in Ref. [70] to evaluate the electronic parameters n , m^* , ξ_0 , and l_e using the values of γ_n , $\xi_{GL}(0)$, and ρ_0 for varying the chemical compositions of $\text{Ta}_x\text{Hf}_{1-x}$. Finally, the effective Fermi temperature (T_F) for $\text{Ta}_x\text{Hf}_{1-x}$ was calculated using the expression [71], where n and m^* are the electronic carrier density and the effective mass of quasiparticles, respectively:

$$k_B T_F = \frac{\hbar^2}{2} (3\pi^2)^{2/3} \frac{n^{2/3}}{m^*}. \quad (12)$$

The values obtained from T_F for each composition lie between 12 000–15 000 K. We have compiled all the estimated electronic parameters of $\text{Ta}_x\text{Hf}_{1-x}$ in Table I. The ratio ξ_0/l_e exceeds the expected range for clean limit superconductivity, indicating that the Ta-Hf binary alloy exhibits dirty limit superconductivity.

IV. PHASE DIAGRAM

The experimental data obtained from the superconducting $\text{Ta}_x\text{Hf}_{1-x}$ binary alloys are summarized in the phase diagram

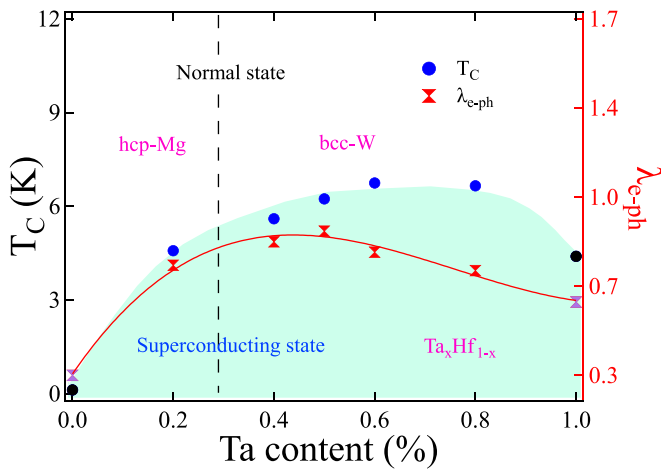


FIG. 5. Superconducting phase diagram of the $\text{Ta}_x\text{Hf}_{1-x}$ alloys. It illustrates the relationship between the superconducting transition temperatures T_C and the electron-phonon coupling λ_{e-ph} , as a function of Ta content. The data for elemental Hf and Ta, depicted, respectively, as a black marker for T_C and a purple marker for λ_{e-ph} , were taken from Refs. [72,73].

shown in Fig 5. As the relative content of Ta and Hf is varied, two crystal structures are observed: *W-bcc* ($Im\bar{3}m$) and *Mg-hcp* ($P6_3/mmc$). At the phase boundary, crystal structure transitions occur between $x = 0.2$ and 0.4 . The highest and lowest values of T_C , 6.7 and 4.5 K, respectively, are obtained for samples with $x = 0.6$ (W cubic-type structure) and $x = 0.2$ (Mg-hcp-type structure) as depicted in Fig. 5. The variation of x on both sides leads to a decrease in the transition temperature, which can be attributed to the influence of elemental Ta and Hf on their respective sides [72,73].

The phase diagram also shows the variation of the electron-phonon coupling constant with the Ta content, exhibiting a dome-like behavior. The three series of BCC alloys ($3d$, $4d$, and $5d$) demonstrate the same dome behavior with a peak at a valence electron/atom ratio $n = 4.5$, a deep minimum near $n = 5.8$, and a shoulder at $n = 6.2$ [66]. The enhanced values of the electron-phonon coupling constant in Ta-Hf binary

alloys are also higher than those of the elemental Hf and Ta, indicating strongly coupled superconductivity.

V. CONCLUSION

This paper presents experimental results focusing on $\text{Ta}_x\text{Hf}_{1-x}$ ($x = 0.2, 0.4, 0.5, 0.6,$ and 0.8) binary alloys. Through powder XRD analysis, it was determined that the crystal structures of $\text{Ta}_x\text{Hf}_{1-x}$ alloys encompass two phases across the entire range of solid solution: *W-bcc* (for $x \geq 0.4$) and *Mg-hcp* (for $x < 0.4$). Investigation of magnetization, electrical transport, and thermodynamic properties revealed that $\text{Ta}_x\text{Hf}_{1-x}$ alloys exhibit superconductivity, with the highest bulk transition temperature observed at $T_C = 6.7$ K for the composition $x = 0.6$. Significantly higher calculated values of the upper critical field $H_{C2}(0)$ were obtained, particularly for $x = 0.2$ and 0.4 , indicating their proximity to the BCS Pauli limiting field. Low-temperature-specific heat data indicated a fully gapped superconducting state, with a larger gap magnitude exceeding the BCS value of 1.76. These unique characteristics suggest possible unconventional behavior, making $\text{Ta}_x\text{Hf}_{1-x}$ alloys intriguing for superconducting device applications. However, further investigations are necessary using microscopic probes, such as nuclear magnetic resonance and muon spin resonance on single/polycrystalline samples. These investigations will provide information on the superconducting pairing mechanism and better understand the possible unconventional nature and anomalous enhancement of the superconducting transition in the $\text{Ta}_x\text{Hf}_{1-x}$ binary alloy.

Note added. We recently learned that a similar observation was reported on Ta-Hf alloys in Ref. [74].

ACKNOWLEDGMENTS

P.K.M. acknowledges the funding agency Council of Scientific and Industrial Research (CSIR), Government of India, for providing the SRF fellowship (Award No: 09/1020(0174)/2019-EMR-I). R.P.S. acknowledges the Science and Engineering Research Board, Government of India, for the Core Research Grant No. CRG/2019/001028.

- [1] J. Bardeen, L. N. Cooper, and J. R. Schrieffer, *Phys. Rev.* **106**, 162 (1957).
- [2] M. Sigrist and K. Ueda, *Rev. Mod. Phys.* **63**, 239 (1991).
- [3] K. Maki, *Phys. Rev.* **148**, 362 (1966).
- [4] G. E. Volovik and L. P. Gor'kov, *Sov. Phys. JETP* **61**, 843 (1985).
- [5] P. W. Anderson, *Phys. Rev. B* **30**, 4000 (1984).
- [6] M. Z. Hasan and C. L. Kane, *Rev. Mod. Phys.* **82**, 3045 (2010).
- [7] N. P. Armitage, E. J. Mele, and A. Vishwanath, *Rev. Mod. Phys.* **90**, 015001 (2018).
- [8] X. L. Qi and S. C. Zhang, *Rev. Mod. Phys.* **83**, 1057 (2011).
- [9] M. Sato and Y. Ando, *Rep. Prog. Phys.* **80**, 076501 (2017).
- [10] R. J. Elliott, *Phys. Rev.* **96**, 280 (1954).
- [11] Arushi, K. Motla, P. K. Meena, S. Sharma, D. Singh, P. K. Biswas, A. D. Hillier, and R. P. Singh, *Phys. Rev. B* **105**, 054517 (2022).
- [12] M. Mandal, C. Patra, A. Kataria, D. Singh, P. K. Biswas, J. S. Lord, A. D. Hillier, and R. P. Singh, *Phys. Rev. B* **104**, 054509 (2021).
- [13] K. P. Sajilesh, D. Singh, P. K. Biswas, Gavin B. G. Stenning, A. D. Hillier, and R. P. Singh, *Phys. Rev. Mater.* **3**, 104802 (2019).
- [14] S. Harada, J. J. Zhou, Y. G. Yao, Y. Inada, and G. Q. Zheng, *Phys. Rev. B* **86**, 220502(R) (2012).
- [15] H. Takeya, M. ElMassalami, S. Kasahara, and K. Hirata, *Phys. Rev. B* **76**, 104506 (2007).
- [16] T. Shang, J. Z. Zhao, D. J. Gawryluk, M. Shi, M. Medarde, E. Pomjakushina, and T. Shiroka, *Phys. Rev. B* **101**, 214518 (2020).
- [17] S. K. P. and R. P. Singh, *Supercond. Sci. Technol.* **34**, 055003 (2021).
- [18] S. K. P., D. Singh, A. D. Hillier, and R. P. Singh, *Phys. Rev. B* **102**, 094515 (2020).

- [19] C. Q. Xu, B. Li, J. J. Feng, W. H. Jiao, Y. K. Li, S. W. Liu, Y. X. Zhou, R. Sankar, N. D. Zhigadlo, H. B. Wang, Z. D. Han, B. Qian, W. Ye, W. Zhou, T. Shiroka, P. K. Biswas, X. Xu, and Z. X. Shi, *Phys. Rev. B* **100**, 134503 (2019).
- [20] S. K. P., D. Singh, P. K. Biswas, A. D. Hillier, and R. P. Singh, *Phys. Rev. B* **98**, 214505 (2018).
- [21] D. Singh, A. D. Hillier, and A. Thamizhavel, and R. P. Singh, *Phys. Rev. B* **94**, 054515 (2016).
- [22] M. Mandal, A. Kataria, C. Patra, D. Singh, P. K. Biswas, A. D. Hillier, T. Das, and R. P. Singh, *Phys. Rev. B* **105**, 094513 (2022).
- [23] R. P. Singh, A. D. Hillier, B. Mazidian, J. Quintanilla, J. F. Annett, D. McK. Paul, G. Balakrishnan, and M. R. Lees, *Phys. Rev. Lett.* **112**, 107002 (2014).
- [24] G. Bian, T. R. Chang, R. Sankar, S. Y. Xu, H. Zheng, T. Neupert, C. K. Chiu, S. M. Huang, G. Chang, I. Belopolski, D. S. Sanchez, M. Neupane, N. Alidoust, C. Liu, B. Wang, C. C. Lee, H. T. Jeng, C. Zhang, Z. Yuan, S. Jia *et al.*, *Nat. Commun.* **7**, 10556 (2016).
- [25] A. P. Place, L. V. Rodgers, P. Mundada, B. M. Smitham, M. Fitzpatrick, Z. Leng, A. Premkumar, J. Bryon, S. Sussman, G. Cheng, T. Madhavan, H. K. Babla, B. Jäck, A. Gyenis, N. Yao, R. J. Cava, N. P. de Leon, and A. A. Houck, *Nat. Commun.* **12**, 1779 (2021).
- [26] R. A. Hein, *Phys. Rev.* **102**, 1511 (1956).
- [27] M. Suenaga and K. M. Ralls, *J. Appl. Phys.* **40**, 4457 (1969).
- [28] J. K. Hulm and R. D. Blaugher, *Phys. Rev.* **123**, 1569 (1961).
- [29] A. Birnboim, *Phys. Rev. B* **14**, 2857 (1976).
- [30] F. J. Morin and J. P. Maita, *Phys. Rev.* **129**, 1115 (1963).
- [31] S. Sundar, L. S. S. Chandra, M. K. Chattopadhyay, S. K. Pandey, D. Venkateswarlu, R. Rawat, V. Ganesan, and S. B. Roy, *New J. Phys.* **17**, 053003 (2015).
- [32] S. Sundar, L. S. Sharath Chandra, M. K. Chattopadhyay, and S. B. Roy, *J. Phys.: Condens. Matter* **27**, 045701 (2015).
- [33] J. M. Corsan and A. J. Cook, *Phys. Lett. A* **28**, 500 (1969).
- [34] W. Gey and D. Kohnlein, *Z. Phys. A: Hadrons Nucl.* **255**, 308 (1972).
- [35] P. Selvamani, G. Vaitheeswaran, V. Kanchana, and M. Rajagopalan, *Physica C* **370**, 108 (2002).
- [36] O. De la Peña-Seaman, R. de Coss, R. Heid, and K.-P. Bohnen, *Phys. Rev. B* **76**, 174205 (2007).
- [37] N. P. de Leon, K. M. Itoh, D. Kim, K. K. Mehta, T. E. Northup, H. Paik, B. S. Palmer, N. Samarth, S. Sangtawesin, and D. W. Steuerman, *Science* **372**, eabb2823 (2021).
- [38] T. G. Berlincourt and R. R. Hake, *Phys. Rev.* **131**, 140 (1963).
- [39] K. M. Wong, E. J. Cotts, and S. J. Poon, *Phys. Rev. B* **30**, 1253 (1984).
- [40] J. Rodríguez-Carvajal, *Physica B* **192**, 55 (1993).
- [41] M. P. Krug, L. L. Oden, and P. A. Romans, *Metall. Trans. A* **6**, 997 (1975).
- [42] K. Ma, K. Gornicka, R. Lefèvre, Y. Yang, H. M. Rønnow, H. O. Jeschke, T. Klimczuk, and F. O. von Rohr, *ACS Mater. Au* **1**, 55 (2021).
- [43] A. A. Castro, O. Olicon, R. Escamilla, and F. Morales, *Solid State Commun.* **255-256**, 11 (2017).
- [44] A. Mani, L. S. Valdhyathan, Y. Hariharan, M. P. Janawadkar, and T. S. Radhakrishnan, *Cryogenics* **36**, 937 (1996).
- [45] M. Matin, L. S. Sharath Chandra, S. K. Pandey, M. K. Chattopadhyay, and S. B. Roy, *Eur. Phys. J. B* **87**, 131 (2014).
- [46] S. L. Narasimhan, R. Taggart, and D. H. Polonis, *J. Nucl. Mater.* **43**, 258 (1972).
- [47] H. Yang, H. Luo, Z. Wang, and H. H. Wen, *Appl. Phys. Lett.* **93**, 142506 (2008).
- [48] R. Prozorov, N. Ni, M. A. Tanatar, V. G. Kogan, R. T. Gordon, C. Martin, E. C. Blomberg, P. P. P. Prommapan, J. Q. Yan, S. L. Budko, and P. C. Canfield, *Phys. Rev. B* **78**, 224506 (2008).
- [49] P. K. Biswas, A. Amato, R. Khasanov, H. Luetkens, K. Wang, C. Petrovic, R. M. Cook, M. R. Lees, and E. Morenzoni, *Phys. Rev. B* **90**, 144505 (2014).
- [50] D. A. Mayoh, J. A. T. Barker, R. P. Singh, G. Balakrishnan, D. McK. Paul, and M. R. Lees, *Phys. Rev. B* **96**, 064521 (2017).
- [51] C. K. Jones, J. K. Hulm, and B. S. Chandrasekhar, *Rev. Mod. Phys.* **36**, 74 (1964).
- [52] N. R. Werthamer, E. Helfand, and P. C. Hohenberg, *Phys. Rev.* **147**, 295 (1966).
- [53] E. Helfand and N. R. Werthamer, *Phys. Rev.* **147**, 288 (1966).
- [54] B. S. Chandrasekhar, *Appl. Phys. Lett.* **1**, 7 (1962).
- [55] A. M. Clogston, *Phys. Rev. Lett.* **9**, 266 (1962).
- [56] A. Kataria, T. Agarwal, S. Sharma, A. Ali, R. S. Singh, and R. P. Singh, *Supercond. Sci. Technol.* **35**, 115008 (2022).
- [57] M. Mandal, K. P. Sajilesh, R. R. Chowdhury, D. Singh, P. K. Biswas, A. D. Hillier, and R. P. Singh, *Phys. Rev. B* **103**, 054501 (2021).
- [58] Arushi, D. Singh, P. K. Biswas, A. D. Hillier, and R. P. Singh, *Phys. Rev. B* **101**, 144508 (2020).
- [59] S. K. P., K. Motla, P. K. Meena, A. Kataria, C. Patra, K. Somesh, A. D. Hillier, and R. P. Singh, *Phys. Rev. B* **105**, 094523 (2022).
- [60] H. Su, T. Shang, F. Du, C. F. Chen, H. Q. Ye, X. Lu, C. Cao, M. Smidman, and H. Q. Yuan, *Phys. Rev. Mater.* **5**, 114802 (2021).
- [61] M. Tinkham, *Introduction to Superconductivity*, 2nd ed. (McGraw-Hill, New York, 1996).
- [62] M. Mandal, S. Marik, K. P. Sajilesh, Arushi, D. Singh, J. Chakraborty, N. Ganguli, and R. P. Singh, *Phys. Rev. Mater.* **2**, 094201 (2018).
- [63] S. Chakraborty, R. Kumar, and N. Mohapatra, *Phys. Rev. B* **107**, 024503 (2023).
- [64] I. K. Dimitrov, N. D. Daniilidis, C. Elbaum, J. W. Lynn, and X. S. Ling, *Phys. Rev. Lett.* **99**, 047001 (2007).
- [65] C. Kittel, *Introduction to Solid State Physics*, 8th ed. (Wiley, Hoboken, NJ, 2005).
- [66] W. L. McMillan, *Phys. Rev.* **167**, 331 (1968).
- [67] T. Shang, D. J. Gawryluk, J. A. T. Verezhak, E. Pomjakushina, M. Shi, M. Medarde, J. Mesot, and T. Shiroka, *Phys. Rev. Mater.* **3**, 024801 (2019).
- [68] R. W. Rollins and Lavern C. Clune, *Phys. Rev. B* **6**, 2609 (1972).
- [69] H. Padamsee, J. E. Neighbor, C. A. Shiffman, *J. Low. Temp. Phys.* **12**, 387 (1973).
- [70] D. Singh, K. P. Sajilesh, Sourav Marik, A. D. Hillier, and R. P. Singh, *Phys. Rev. B* **99**, 014516 (2019).
- [71] A. D. Hillier and R. Cywinski, *Appl. Magn. Reson.* **13**, 95 (1997).
- [72] T. Mamiya, K. Nomura, and Y. Masuda, *J. Phys. Soc. Jpn.* **28**, 380 (1970).
- [73] J. J. Hopfield, *Phys. Rev.* **186**, 443 (1969).
- [74] T. Klimczuk, S. Krolak, and R. J. Cava, *Phys. Rev. Mater.* **7**, 064802 (2023).